



Radiation Hydrodynamical Turbulence in Protoplanetary Disks: Numerical Models and Observational Constraints

Mario Flock^{1,2} , Richard P. Nelson^{2,3}, Neal J. Turner^{1,2} , Gesa H.-M. Bertrang^{4,5}, Carlos Carrasco-González⁶, Thomas Henning⁷, Wladimir Lyra^{1,8} , and Richard Teague^{7,9}

¹ Jet Propulsion Laboratory, California Institute of Technology, Pasadena, California 91109, USA; mflock@caltech.edu

² Kavli Institute For Theoretical Physics, University of California, Santa Barbara, CA 93106, USA

³ Astronomy Unit, Queen Mary University of London, Mile End Road, London E1 4NS, UK

⁴ Universidad de Chile, Departamento de Astronomía, Casilla 36-D, Santiago, Chile

⁵ Millennium Nucleus Protoplanetary Disks in ALMA Early Science, Universidad de Chile, Casilla 36-D, Santiago, Chile

⁶ Instituto de Radioastronomía y Astrofísica UNAM, Apartado Postal 3-72 (Xangari), 58089 Morelia, Michoacán, México

⁷ Max-Planck-Institut für Astronomie, Königstuhl 17, D-69117 Heidelberg, Germany

⁸ Department of Physics and Astronomy, California State University Northridge, 18111 Nordhoff Street, Northridge, CA 91330, USA

⁹ Department of Astronomy, University of Michigan, 311 West Hall, 1085 S. University Avenue, Ann Arbor, MI 48109, USA

Received 2017 August 8; revised 2017 October 12; accepted 2017 October 13; published 2017 November 27

Abstract

Planets are born in protostellar disks, which are now observed with enough resolution to address questions about internal gas flows. Magnetic forces are possibly drivers of the flows, but ionization state estimates suggest that much of the gas mass decouples from magnetic fields. Thus, hydrodynamical instabilities could play a major role. We investigate disk dynamics under conditions typical for a T Tauri system, using global 3D radiation-hydrodynamics simulations with embedded particles and a resolution of 70 cells per scale height. Stellar irradiation heating is included with realistic dust opacities. The disk starts in joint radiative balance and hydrostatic equilibrium. The vertical shear instability (VSI) develops into turbulence that persists up to at least 1600 inner orbits (143 outer orbits). Turbulent speeds are a few percent of the local sound speed at the midplane, increasing to 20%, or 100 m s^{-1} , in the corona. These are consistent with recent upper limits on turbulent speeds from optically thin and thick molecular line observations of TW Hya and HD 163296. The predominantly vertical motions induced by the VSI efficiently lift particles upward. Grains 0.1 and 1 mm in size achieve scale heights greater than expected in isotropic turbulence. We conclude that while kinematic constraints from molecular line emission do not directly discriminate between magnetic and nonmagnetic disk models, the small dust scale heights measured in HL Tau and HD 163296 favor turbulent magnetic models, which reach lower ratios of the vertical kinetic energy density to the accretion stress.

Key words: accretion, accretion disks – hydrodynamics – protoplanetary disks – radiative transfer – turbulence

1. Introduction

Understanding the transport of angular momentum and the underlying dynamics in protoplanetary disks is one of the key questions in planet and star formation research. Since classical α -disk theory was presented by Shakura & Sunyaev (1973), in which the transport is described by an effective turbulent viscosity, there has been an ongoing search for a mechanism capable of generating turbulence in accretion disks, as pure molecular viscosity is inefficient at transporting angular momentum (Pringle 1981). One powerful mechanism providing turbulence is the magnetorotational instability (Balbus & Hawley 1991, 1998). However, recent theoretical studies have shown that magnetically driven instabilities can be suppressed in some regions of the disk (Turner et al. 2014; Armitage 2015), due to the different non-ideal terms of Ohmic resistivity, ambipolar diffusion, and Hall drift (Wardle 2007; Salmeron & Wardle 2008; Bai 2011, 2014; Dzyurkevich et al. 2013). In such regions, hydrodynamical instabilities could play an important role. Examples include the Goldreich–Schubert–Fricke (GSF) instability (Goldreich & Schubert 1967; Fricke 1968), the convective instability (Cameron & Pine 1973), the Papaloizou–Pringle instability (Papaloizou & Pringle 1984), the baroclinic instability (Klahr & Bodenheimer 2003; Lesur & Papaloizou 2010), the Loren-Bate instability (Lorén-Aguilar & Bate 2015), the convective overstability

(Klahr & Hubbard 2014; Lyra 2014), the zombie vortex instability (Marcus et al. 2013, 2015; Lesur & Latter 2016; Umurhan et al. 2016), or the spiral wave instability (Bae et al. 2016), which could appear in self-gravitating disks or in disks perturbed by a massive planet (Pohl et al. 2015). The GSF, first considered as acting on stellar interiors, is now of interest for accretion disks (Urpin & Brandenburg 1998; Urpin 2003; Arlt & Urpin 2004). In particular, it may operate in protostellar disks’ outer regions, where thermal relaxation is faster than the orbital rotation (Nelson et al. 2013; Lin & Youdin 2015). In this context, the instability is known as the vertical shear instability, or VSI. Hydrodynamical calculations indicate that the VSI produces stress-to-pressure ratios, α , ranging from $\sim 10^{-3}$ with an isothermal equation of state (Nelson et al. 2013), down to 10^{-4} when considering detailed radiative heating and cooling (Stoll & Kley 2016).

Recent high-resolution observations of protoplanetary disks at millimeter wavelengths have revealed astonishing substructures in the thermal dust emission (ALMA Partnership et al. 2015; Andrews et al. 2016; Carrasco-González et al. 2016; Isella et al. 2016; Fedele et al. 2017; Macías et al. 2017). For the first time, the disk scale height (approx. 10 au at a distance to the star of 100 au) is resolved. Detailed radiative transfer models of these systems (Pinte et al. 2016; Liu et al. 2017; van Boekel et al. 2017) support a small stress-to-pressure ratio of $\alpha \ll 0.01$, based on best-fit models of the dust disk

scale height in the disk system HL Tau. An opportunity to obtain observational constraints on the magnetic field in disks could be the measurements of the linearly polarized continuum and line emission. Recent ALMA observations of HD 142527 present polarization maps at 0.874 mm (Kataoka et al. 2016) with 70 au resolution. Those maps show a clear radial symmetry structure inside a radius of 150 au, with a polarization degree strength between 0.1% and 14%. Both the radial pattern and the degree of the polarization of this observation match very well with the results of thermal dust polarization radiation transfer models from 3D non-ideal MHD models (Bertrang & Wolf 2017; Bertrang et al. 2017) based on the simulation results of Flock et al. (2015). However, dust scattering also plays an important role (Kataoka et al. 2015, 2017), especially in regions where the radiation field becomes anisotropic, which happens close to the optical depth $\tau = 1$ transition and where the radiation field can induce grain alignment (Tazaki et al. 2017). Direct evidence for magnetic fields in disks based on these constraints is still missing.

The kinematics in disks have also been measured directly. One of the first indications of subsonic turbulence in protoplanetary disks was found by the SMA and PdBI telescopes for the systems TW Hya and HD 163296 (Hughes et al. 2011) and for DM Tau (Guilloteau et al. 2012). New observational constraints on the disk kinematics with ALMA confirm subsonic turbulent velocities in the disk (Flaherty et al. 2015, 2017; Teague et al. 2016). In this work we present new high-resolution global radiation hydrodynamic models of the outer protoplanetary disk. Together with our previous magnetic disk models (Flock et al. 2015) we will compare both sets of simulation results with the recently obtained observational constraints and determine which model fits best. The new radiation hydrodynamic stratified disk simulations include irradiation by the star and realistic dust opacities, and achieve a resolution of over 70 cells per disk scale height. Compared to previous models, this work achieves three main advances: (1) realistic initial conditions that are in full radiation hydrostatic equilibrium, (2) radiation hydrodynamic simulations with realistic heating and cooling, and (3) high resolution with a high-order numerical scheme.

In this work we compare high-resolution global radiation hydrodynamic models with these recently obtained observational constraints.

The structure of the paper is as follows. In Section 2 we present the method, the equations, and the initial conditions in hydrostatic equilibrium. In Section 3 we present the simulation results and compare the model with recent observational constraints. Sections 4 and 5 provide a discussion and conclusions.

2. Numerical Method and Disk Model

The radiation hydrodynamic equations are solved using the hybrid flux-limited diffusion and irradiation method developed by Flock et al. (2013) as implemented in the current version 4.2 of the PLUTO code (Mignone et al. 2007). For this work we choose the high-order piece-wise parabolic method, the Harten–Lax–Van Leer approximate Riemann Solver with the contact discontinuity (HLLC), the FARGO scheme (Masset 2000; Mignone et al. 2012), and the Runge–Kutta time integrator. The Courant number is set to 0.3. This configuration provides very low intrinsic numerical dissipation, which is favored for simulating hydrodynamic instabilities. The

equations solved are

$$\frac{\partial \rho}{\partial t} + \nabla \cdot [\rho \mathbf{v}] = 0, \quad (1)$$

$$\frac{\partial \rho \mathbf{v}}{\partial t} + \nabla \cdot [\rho \mathbf{v} \mathbf{v}^T] + \nabla P = -\rho \nabla \Phi, \quad (2)$$

$$\begin{aligned} \frac{\partial E}{\partial t} + \nabla \cdot [(E + P) \mathbf{v}] = & -\rho \mathbf{v} \cdot \nabla \Phi \\ & - \kappa_P \rho c (a_R T^4 - E_R) \\ & - \nabla \cdot F_*, \end{aligned} \quad (3)$$

$$\frac{\partial E_R}{\partial t} - \nabla \cdot \frac{c \lambda}{\kappa_R(T) \rho} \nabla E_R = \kappa_P(T) \rho c (a_R T^4 - E_R), \quad (4)$$

with the density ρ , the velocity vector \mathbf{v} , the gas pressure

$$P = \frac{\rho k_B T}{\mu_g u}, \quad (5)$$

the gas temperature T , the mean molecular weight μ_g , the Boltzmann constant k_B , the atomic mass unit u , the total energy $E = \rho \epsilon + 0.5 \rho \mathbf{v}^2$, and the gas internal energy per unit volume $\rho \epsilon$. The closure relation between gas pressure and internal energy is provided by $P = (\Gamma - 1) \rho \epsilon$, with the adiabatic index Γ . Other symbols include the radiation energy E_R , the irradiation flux F_* , the Rosseland and Planck opacities σ_R and σ_P , the radiation constant $a_R = 4\sigma_b/c$, the Stefan–Boltzmann constant σ_b , and c as the speed of light. The flux limiter

$$\lambda = \frac{2 + R}{6 + 3R + R^2} \quad (6)$$

is taken from Levermore & Pomraning (1981, Equation (28) therein) with

$$R = \frac{|\nabla E_R|}{\sigma_R E_R}. \quad (7)$$

The gas is a mixture of molecular hydrogen and helium with solar abundance (Decampli et al. 1978) so that $\mu_g = 2.35$ and $\Gamma = 1.42$. In this work we consider the frequency-integrated irradiation flux at a radial distance r to be

$$F_*(r) = \left(\frac{R_*}{r} \right)^2 \sigma_b T_*^4 e^{-\tau}, \quad (8)$$

with T_* and R_* being the surface temperature and radius of the star. The radial optical depth for each meridional height θ of the irradiation flux is given by

$$\begin{aligned} \tau_*(r, \theta) &= \int_{R_*}^r \kappa(T_*) \rho_{\text{dust}}(r, \theta) dr \\ &= \tau_0 + \int_{R_0}^r \kappa(T_*) \rho_{\text{dust}}(r, \theta) dr, \end{aligned} \quad (9)$$

where R_0 denotes the inner radius of the computational domain. The quantity τ_0 is the inner optical depth provided by material located between the surface of the star and R_0 , with $\tau_0 = \kappa_* \rho_{R_0} (R_0 - 3R_*)$.

We define two opacities, one to the starlight $\kappa_* = 1300 \text{ cm}^2 \text{ g}^{-1}$, and the other to the disk's thermal re-emission $\kappa_d = 400 \text{ cm}^2 \text{ g}^{-1}$. These are Planck-weighted averages of the frequency-dependent dust opacity, respectively at the stellar

Table 1

Setup Parameters for the 3D Radiation HD Disk Models, Including the Gas Surface Density, the Stellar Parameters, the Opacities for Stellar Irradiation, and Thermal Emission

Surface density	$\Sigma = 6.0 \left(\frac{r}{100 \text{ au}} \right)^{-1} \text{ g cm}^{-2}$
Stellar parameters	$T_* = 4000 \text{ K}, R_* = 2.0 R_\odot, M_* = 0.5 M_\odot$
Opacities	$\kappa_* = 1300 \text{ cm}^2 \text{ g}^{-1}$ $\kappa_d = 400 \text{ cm}^2 \text{ g}^{-1}$

temperature and a typical re-emission color temperature of 300 K. The opacities are measured in cross sections per unit mass of dust, and are listed in Table 1.

2.1. Boundary Condition and Buffer Zone

For all models, we use a modified outflow boundary condition, which enforces zero inflow at the radial and θ boundaries. In addition, we extrapolate the logarithmic density along the meridional direction into the ghost zones. In the radial direction we apply buffer zones: a surface density relaxation from 20 to 22 au to the initial profile and a radial velocity damping from 20 to 21 au and from 97 to 100 au to zero velocity. In the absence of these buffers the emptying of the disk would affect the irradiation layer and hence the temperature in the disk. These buffer zones are excluded when we present our kinematic analysis of the results.

2.2. Initial Conditions

For the initial condition, we follow the approach by Flock et al. (2013) and construct a set of 2D axisymmetric profiles of density, temperature, and rotation velocity, which are in radiation hydrostatic equilibrium. For the star and disk parameters, we use a model that has been applied to explain various spatially resolved multi-band observations of proto-stellar disks (Wolf et al. 2003, 2008; Schegerer et al. 2008, 2009; Sauter et al. 2009; Liu et al. 2012; Madlener et al. 2012; Gräfe et al. 2013). The model uses the parameters of a typical T Tauri system. For example, similar density and temperature profiles are found in the TW Hya disk, as discussed in Section 4. The star and disk parameters are summarized in Table 1. We assume a total dust-to-gas mass ratio of 10^{-2} . Furthermore, we consider the dust-to-gas mass ratio of small grains ($a = 0.1\text{--}10 \mu\text{m}$), which is relevant for the disk cooling (and thermal opacity), to be 10^{-3} and 10^{-4} , which is reflected in the model names. Figure 1 shows the initial temperature profile for reference model M3. We note again that the dust-to-gas mass ratio in the model name is relevant for determining the opacity of the thermal emission. We assume the dust mass of small grains, which is relevant for the infrared emission, has been reduced due to dust growth (Birnstiel et al. 2012; Flock et al. 2013). The dust-to-gas mass ratio directly controls the local opacity and thus the thermal equilibrium timescale. Model M3 presents a 10 times higher dust-to-gas mass ratio for the small grains, compared to model M4. However, both models display the short thermal equilibration timescales required for the VSI to operate (Lin & Youdin 2015).

2.3. Thermal Timescale and Critical Timescale for the VSI

We calculate the detailed cooling timescales for both initial models and compare them with the critical timescale required

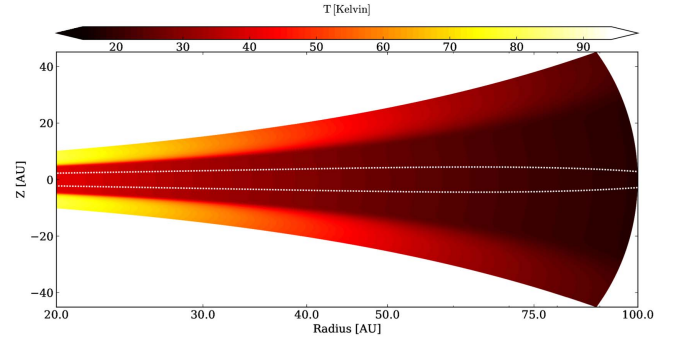


Figure 1. Initial 2D temperature profiles in the R - Z plane for model M3. The temperature rise at the surface marks the surface of unit starlight optical depth. The dotted line shows the surface of vertically integrated optical depth unity for the thermal emission.

for the VSI to operate. The maximum thermal equilibration timescale consistent with VSI is

$$t_c = \frac{h|q|}{\gamma - 1} \quad (10)$$

(Lin & Youdin 2015), where q is the radial temperature profile exponent and $h = H/R$ is the ratio of the disk scale height to the radius. The thermal relaxation timescale can be estimated by looking at the timescales in the optically thin and thick limits. In the optically thin regime, the corresponding length scale of the radiation transport is given by the mean free path of the photons

$$l_{\text{thin}} = \frac{1}{\kappa_{\text{dg}} \rho}, \quad (11)$$

which is typically given by the available dust density ρ_d and dust opacity κ_d per gram of gas mass $\kappa_{\text{dg}} = \kappa_d \frac{\rho_d}{\rho}$.

The radiation diffusion coefficient can be written as

$$D_{\text{rad}} = \frac{16\sigma_b T^3}{3\kappa_{\text{dg}} \rho^2 C_v}, \quad (12)$$

with the specific heat capacity at constant volume C_v .

Following Lin & Youdin (2015), the thermal relaxation timescale can be approximated as the sum of the relaxation timescales in the optical thin and thick regime with

$$t_{\text{relax}} = t_{\text{thin}} + t_{\text{thick}} = \frac{l_{\text{thin}}^2}{3D_{\text{rad}}} + \frac{H^2}{D_{\text{rad}}}, \quad (13)$$

using the disk scale height H as the typical perturbation length scale.

Using this, the optically thin and thick relaxation timescales, normalized by Ω_K , are given by

$$\tau_{\text{relax}} = \tau_{\text{thin}} + \tau_{\text{thick}} = \frac{C_v \Omega_K}{16\sigma_b T^3} \left[\frac{1}{\kappa_{\text{dg}}} + 3H^2 \rho^2 \kappa_{\text{dg}} \right]. \quad (14)$$

Figure 2 compares the critical timescale, t_c , for the VSI with the disk thermal timescales for our model. The plot shows that the thermal equilibration timescales are lower than the critical timescale and the VSI is expected to operate in the full domain. We note that for model M3, the dominant timescale at the midplane is given by the radiation diffusion, while for model M4, the dominant timescale is given in the optical thin limit.

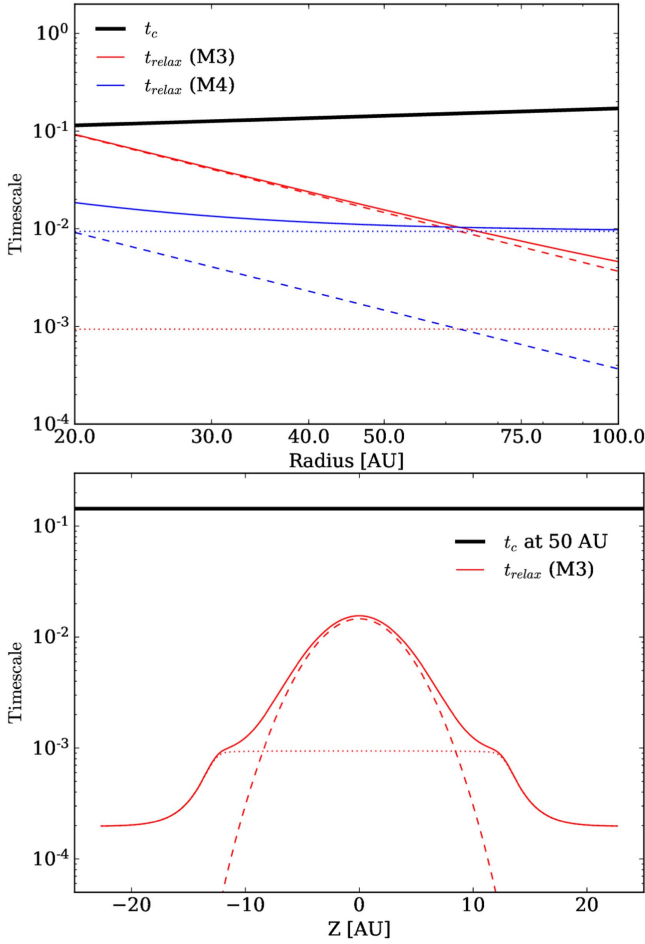


Figure 2. Top: radial profiles of the critical timescale for the VSI (black) and the relaxation timescales at the midplane in models M3 (red) and M4 (blue). All values are in units of the local inverse Keplerian frequency. Bottom: relaxation timescale vs. height at 50 au in model M3. Both panels also show the optically thin (dotted line) and optically thick (dashed line) limits.

We note that local enrichment and depletion of dust grains could lead to variations of the thermal timescales.

These considerations mean the VSI could in principle operate in model M3 down to 19 au, a little closer to the star than the domain’s innermost radius of 20 au. This agrees well with work by Malygin et al. (2017), where the zone of VSI operation based on the radiative relaxation timescale lies between 15 and 180 au for disk density and temperature profiles similar to our model M3. For model M4 the unstable region extends to a radius inward of 7 au. This shows that dust-depleted atmospheres in a protoplanetary disk could support the conditions needed for the VSI to operate over a large radial extent. In addition, we expect the upper layers of the disk to have conditions conducive to the VSI (noting, however, that we neglect the possible stabilizing effects of magnetic fields in this work).

3. Simulation Results and Comparison with Observations

In this section we present the results for the disk dynamics and the turbulent structure. We first investigate the effect of changing the dust-to-gas mass ratio and hence the local opacity, using M3 and M4. In Section 3.1 we investigate the turbulent characteristics of the two models. In Section 3.2 we summarize recent constraints from measurements of molecular line-

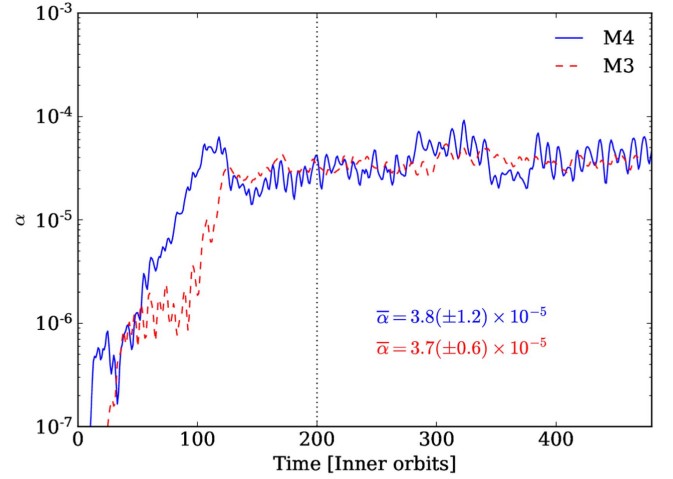


Figure 3. Time evolution of the stress-to-pressure ratio α in the two models. Also listed are time averages from 200 inner orbits up through the end of each calculation.

broadening. In Section 3.3 we analyze how grains of representative sizes move in the two models, we determine their dust scale heights from our simulations, and compare them to recent best-fit models of HL Tau by Pinte et al. (2016).

3.1. Stress-to-pressure Ratio

We determine the strength of the turbulence by calculating the stress-to-pressure ratio α . For these radiation hydrodynamic models the Reynolds stress $T_{r\phi}$ is the relevant stress that enables transport of angular momentum. We find a typical value by volume-averaging the mass-weighted stress-to-pressure ratio, using

$$\alpha = \frac{\int \rho \left(\frac{T_{r\phi}}{P} \right) dV}{\int \rho dV} = \frac{\int \rho \left(\frac{\rho v_\phi^2}{P} \right) dV}{\int \rho dV}. \quad (15)$$

We choose mass-weighting for direct comparison with measurements from our magnetohydrodynamical disk models. We compare this approach with a simple ratio of volume-averaged stress to volume-averaged pressure, as in Nelson et al. (2013), in Appendix A. The two approaches deliver similar results.

The time evolution of the stress-to-pressure ratio α is presented in Figure 3 for both models. After around 100 inner orbits, the value of α saturates and both models show a steady turbulent evolution. Both models show nearly the same saturated value of α . For model M3 we determine a time-averaged value of 3.7×10^{-5} , compared to 3.8×10^{-5} for model M4. The time average is done between 200 inner orbits until the end of the simulation run. We note that the fluctuations in the stress-to-pressure ratio around the mean remain small and at a level of 30%. Table 2 summarizes the results.

The results of a long-term evolution are presented in Appendix A, performed for model M4 for over 1600 inner orbits. We note that there is a very stable and steady turbulent evolution. Snapshots of the turbulent velocity field in steady-state are shown in Figure 4 for both models. The 3D rendering shows the characteristic turbulent structure of the VSI, showing enhanced turbulent motions with a velocity dispersion up to

Table 2
List of Simulations and Model Parameters

Model Name	$\rho_{\text{dust}}/\rho_{\text{gas}}$	Domain Size: $R_{\text{in}}-R_{\text{out}}$: Z/R : Φ_{max}	Resolution ($N_r \times N_\theta \times N_\phi$)	$\bar{\alpha}$	Runtime [Orbits at 20 au]
M3	10^{-3}	20–100 au: ± 0.35 : 0.392 rad (22°5)	$1024 \times 512 \times 256$	$3.7(\pm 0.6) \times 10^{-5}$	470
M4	10^{-4}	20–100 au: ± 0.35 : 0.392 rad (22°5)	$1024 \times 512 \times 256$	$3.8(\pm 1.2) \times 10^{-5}$	1610

Note. From left to right: the model name, the dust-to-gas mass ratio, the domain size, the resolution, the space- and time-averaged stress-to-pressure ratio, and the total simulation runtime.

100 m s^{-1} in the disk corona. At the midplane the turbulent velocities are around 10 m s^{-1} and below. We emphasize again that model M3 and model M4 show very similar turbulent behavior. The largest differences that we observe are that the turbulent velocities at the midplane are slightly reduced compared to model M3. This can already be seen by looking at the snapshots of Figure 4. Furthermore, in model M4 we observe an increase of turbulent velocity slightly earlier with height. These differences might be connected to the different temperature profile, as in model M4 in which the irradiation heating zone reaches much deeper into the disk due to the lower optical depth. In the following analysis we will focus on model M3.

3.2. Kinematic Constraints from Line Observations

In this section we review recent observational constraints and compare them with the results from our radiation hydrodynamic simulations.

In the left panel of Figure 5, we summarize the model results and compare them with the observational constraints. The plot shows the time and spatially averaged turbulent velocity profile over height for model M3. The turbulent velocity in the $r - \theta$ plane is measured using

$$\langle \overline{v_{\text{rms}}(r, \theta)} \rangle = \langle \sqrt{(v_r - \overline{v_r})^2 + (v_\theta - \overline{v_\theta})^2 + (v_\phi - \overline{v_\phi})^2} \rangle, \quad (16)$$

with the overbarred quantities representing the azimuthal average and the symbols $\langle \rangle$ representing the time average. In addition, we calculate the turbulent velocity of the v_θ component only using $\langle \overline{v_{\text{rms}}^\theta(r, \theta)} \rangle = \langle \sqrt{(v_\theta - \overline{v_\theta})^2} \rangle$. This case is useful to compare with face-on disk observations in which one is sensitive for only the vertical velocity component. The same approach is used to calculate the standard deviation. For each time output we calculate the standard deviation in the (r, θ) plane along the ϕ direction. In a second step we perform the time average of this spatial standard deviation. The results are presented at the radius of 50 au using a radial average of ± 1 disk scale height. Figure 5's left panel shows that the turbulent velocity at the midplane is around $0.01(\pm 0.007)c_s$, while the turbulent velocity increases until reaching a quasi-plateau with $0.06(\pm 0.04)c_s$. We note that, depending on the optical thickness of the line and the local abundance of the molecule, the observations trace different regions inside the disk. The pure vertical component of the turbulent velocity lies slightly below; see the dashed line in Figure 5. We also checked for the radial dependence and determined the profiles at 30 and 70 au. We found that the turbulent velocity slightly increases with radius. At 30 au the turbulent velocities were reduced by

around 30%, while at 70 au they were increased by around 50% compared to the values at 50 au.

By carefully investigating for CO, CN, and CS observations of the disk system TW Hya, Teague et al. (2016) found an upper limit of the turbulence causing line-broadening, consistent with $v_{\text{turb}} \leq 0.2c_s$. Another ALMA observation of the disk HD 163296 in different CO lines by Flaherty et al. (2015) supports the general finding of relatively low turbulent velocities in the disk. They found an upper limit of around $v_{\text{turb}} \leq 0.04c_s$ for optical thin tracers, which are sensitive to the turbulence at the midplane (Flaherty et al. 2017), like in the case for DCO+.

Figure 5's left panel shows that the results of our radiation hydrodynamic simulations are consistent with the observations of Teague et al. (2016) and Flaherty et al. (2015), which support the idea of a disk with a relatively low turbulent velocity. The midplane and the upper layers lie within the upper limits presented by Teague et al. (2016). For this comparison, we include our previous magnetized disk simulations presented in Flock et al. (2015). In Figure 5, right panel, we re-analyze the data set published by Flock et al. (2015) using model D2G_e-2, taking the same spatial average and position as described above. In the magnetized model, the turbulent velocities are substantially increased, in the midplane region as well as in the low-density upper layers. Starting at a height above $Z/R > 0.25$, which corresponds to $Z > 12.5$ au, the turbulent velocity of the vertical component is still consistent with the proposed upper limit by Teague et al. (2016) found for TW Hya. We note that ambipolar diffusion might reduce the turbulent activity, especially in the upper layers of magnetized disks as shown by Simon et al. (2015b), and thus reduce the turbulent broadening of molecular line emission (Simon et al. 2015a). The details of the region of emission depend mainly on the observed molecule. For TW Hya, Teague et al. (2016) found the emission from ^{12}CO to occur at a height $Z/R \sim 0.3-0.4$, from ^{13}CO at a height $Z/R \sim 0.2$, while the emission from the less optically thick isotopologue C^{18}O traced a height $Z/R \lesssim 0.2$. Observations and models of HD 142527 predict the CO line to originate from a height of about 1 au at a radius of 100 au (Perez et al. 2015), which would basically trace the midplane turbulence. Detailed modeling using line radiation transfer and chemistry will be necessary to further constrain the disk regions responsible for the line emission.

We summarize that the upper limits on the turbulent velocity found in the system TW Hya (Teague et al. 2016) and HD 163296 (Flaherty et al. 2015) are both consistent with the disk midplane turbulent velocities by magnetized and non-magnetized disk models.

The turbulent velocity found in the disk atmosphere in magnetized models with Ohmic dissipation only are too large to be consistent with observations of turbulent line-broadening. Further inclusion of ambipolar diffusion could reduce the

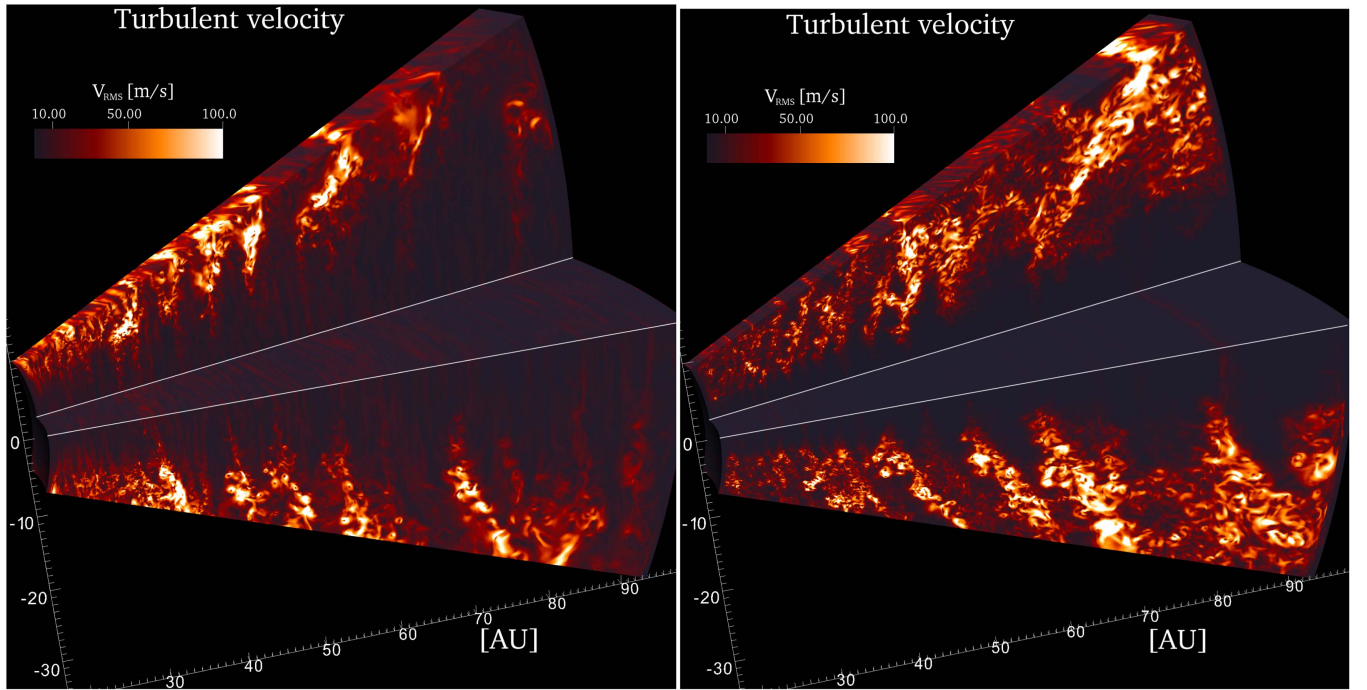


Figure 4. 3D rendering of turbulent speeds in model M3 after 440 inner orbits (left) and model M4 after 1000 inner orbits (right). In both cases, we see the near side of the domain’s lower half, and the far side of its upper half. The rest of the upper half is cut away to reveal values on the midplane. The turbulent velocity is 10 m s^{-1} in the midplane, but exceeds 100 m s^{-1} at some points in the corona.

turbulence to levels consistent with observations. The kinematics of the disk atmosphere is traced by optically thick tracers like ^{12}CO or ^{13}CO . Here, Flaherty et al. (2017) found values for HD 163296 that would be more consistent with the non-magnetized model M3, while the predictions for TW Hya (Teague et al. 2016) would compare well with results from both our magnetized and non-magnetized models.

3.3. Dust Dynamics and Scale Height

In this section we measure the vertical dust distribution obtained in the simulations and compare it with recent observational constraints. In model M3 we introduce dust grains with sizes of $100 \mu\text{m}$ and 1 mm . The dust grains are spherical and have a solid density of 3 g cm^{-3} . For this model we consider the Epstein gas drag regime for the particles and the coupling time t_s becomes

$$t_s = \frac{\rho_d a}{\rho_g c_s}, \quad (17)$$

with the solid density ρ_d , the grain size a , the gas density ρ_g , and the sound speed c_s . For example, grains 1 mm in size have Stokes number $\text{St} = t_s \Omega_K = 0.053$ in the midplane at 50 au and thus are only moderately coupled to the gas. We note that the stopping time for both particle sizes is well resolved. The particle motion is solved using a Lagrangian method based on the equation of motion in the spherical coordinates system. For more details on the particle motion routine we refer to the Appendix section by Ruge et al. (2016). We place a total of one million particles equally distributed over two sizes, and uniformly distributed in the $r-\phi$ plane at the midplane. The initial velocity of the particles is set to match the local Keplerian velocity. The dust grains are distributed at the

midplane between 25 and 95 au . The particles are introduced at a time when the VSI turbulence is already in a steady-state after 400 inner orbits. To measure the vertical distribution, we consider all particles in the radial bin between 25 and 35 au . We sample the grains by creating a high-resolution grid with 1000 cells in the vertical direction. This grid vertical extent is arbitrarily chosen to include all the grains for the given radial bin. The distribution is averaged for multiple time snapshots after they have relaxed to a new state; see Appendix B. The results are summarized for the two grain sizes in the left panel of Figure 6. The $100 \mu\text{m}$ grains present a vertical distribution similar to the gas. The 1 mm grains are mixed less efficiently. Their profile shows a quasi-plateau with a dropoff above one gas scale height. This extent of the plateau matches the extent of the vertical bulk motions created by the VSI, which appear within one scale height above and below the disk midplane. These large-scale vertical oscillations move the bulk of the 1 mm grains up and down. These vertical motions are illustrated in Figure 7. The left panel of Figure 7 shows characteristic vertical motions of the disk bulk material of around 50 m s^{-1} at the disk midplane for model M3. Those motions easily overshoot the midplane region, which emphasizes the need for fully stratified models of both hemispheres. In contrast, the corresponding magnetized model by Flock et al. (2015) shows turbulent motions with smaller amplitudes at the midplane compared to model M3. In Appendix C we present snapshots of the grains in the $R-Z/R$ plane to show the characteristic vertical motions. We also note that for the given time average, only small numbers of particles are leaving and entering the radial region used to undertake the average due to radial drift, therefore this should not affect the results.

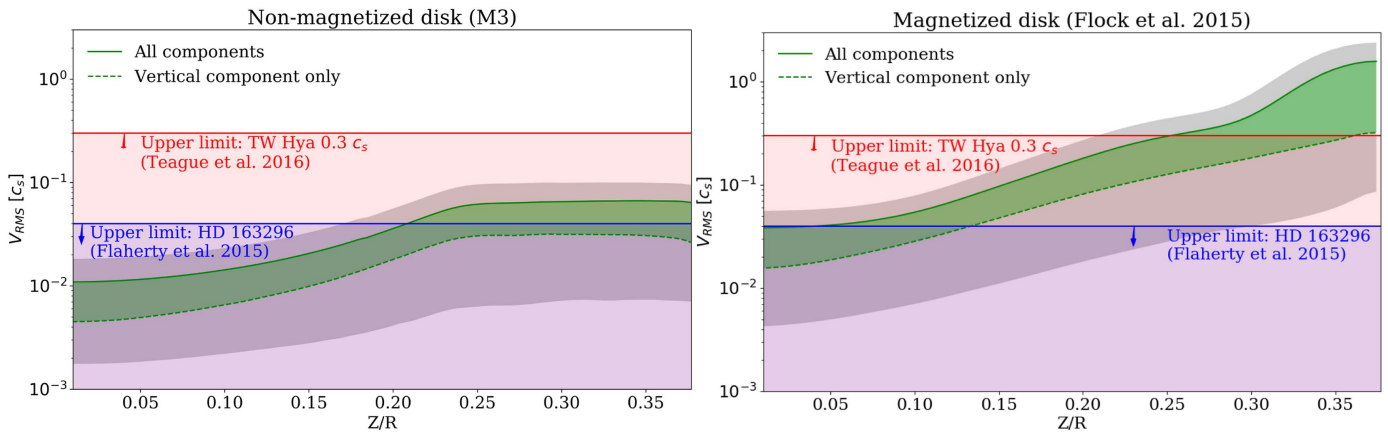


Figure 5. Left: time- and space-averaged profile of the turbulent velocity over height for model M3. Right: time- and space-averaged profile of the turbulent velocity over height for magnetized disk model by Flock et al. (2015). Both profiles show the values at 50 au. The best-fit constraints from the systems TW Hya (Teague et al. 2016) and HD 163296 (Flaherty et al. 2015) are annotated. The green area presents the range of turbulent velocity, for the vertical component only (dashed line) and for all velocity components (solid line). The gray area shows the standard deviation for each component over horizontal planes, averaged in time.

In the following, we present and compare the results with our previous magnetized disk models by Flock et al. (2015) and Ruge et al. (2016). These models share the same stellar and disk parameters as used for this work. In addition to the hydrodynamics, those models solve for the magnetohydrodynamics by considering an initial vertical magnetic field and a 2D r - θ profile of Ohmic resistivity. Magnetic forces redistribute gas to form a local pressure maximum at the edge of the dead zone, where Ohmic diffusion shuts off magnetorotational turbulence. Gas at the pressure maximum orbits exactly at Keplerian speed, halting the headwind-induced inward drift of particles marginally coupled to the outer sub-Keplerian gas by drag. In addition, the gas within the dead zone, being magneto-rotationally stable, is only weakly turbulent. For these MHD models we analyze the vertical distributions of the grains nearest in size to those we modeled here. These are 0.9 and 1.7 mm in radius, and were trapped between 40 and 50 au. The results are summarized in the right panel of Figure 6. The particle vertical distribution fits very well with the best-fit model by Pinte et al. (2016), which determined the vertical scale height for mm-sized grains in HL Tau to $H_{\text{dust}}/R = 0.007$ at 100 au. The vertical distribution of the 1.7 mm and 0.9 mm grains that are trapped inside the pressure bump lie perfectly in between the best-fit value by Pinte et al. (2016).

We conclude that the vertical mixing of grains by the VSI is fundamentally different from the mixing induced by MHD turbulence in the upper layers of protoplanetary disks. The modes that are excited in a VSI-unstable disk have very little structure in the vertical direction compared to the radial direction (i.e., $k_z/k_R \ll 1$, where k_z and k_R are the vertical and radial wave numbers), leading to the efficient lofting of grains away from the midplane and a large effective diffusion coefficient for the vertical mixing of grains. For HL Tau, the vertical scale height of 1 mm dust grains was fitted to be small and of the order of $H/R = 0.007$. Our models of grains embedded in a VSI turbulent disk reveal a much larger scale height, close to the gas disk scale height. For HL Tau and HD 163296 such a high dust scale height can be ruled out, as otherwise the gaps would not become visible (Isella et al. 2016; Pinte et al. 2016). In contrast, our previous global MHD simulations of a T Tauri system present a dust scale height of mm-sized grains of $H/R = 0.007$. Those grains are trapped in

a ring and they experience relatively low levels of turbulent mixing due to the low ionization degree and hence poor gas-magnetic coupling. In summary, it appears that the small turbulent velocities inferred for the outer regions of protoplanetary disks from molecular line observations, combined with the high levels of vertical settling inferred for mm-sized grains, are best explained using a disk model in which non-ideal effects allow low levels of MHD turbulence to be present, but with sufficient magnetic coupling that the VSI is largely suppressed.

3.4. Dust Continuum Observations

In the following, we perform Monte-Carlo radiation transfer post-processing of our simulation results with RADMC-3D (Dullemond 2012). We normalize the dust densities obtained from the radiation-hydrodynamics calculations assuming a global dust-to-gas mass ratio of 1%, spread over a power-law grain size distribution from 0.1 μm to 1 mm. The dust density is sampled using three dust bins, a small grain bin with a smooth size distribution from 0.1 to 10 μm , and two large grain bins with single sizes of 100 μm and 1000 μm . To distribute and sample the total dust mass over the bins we follow the prescription presented by Ruge et al. (2016; Appendix A therein), using the power-law index of -3.5 to determine the size distribution. Figure 8 shows a snapshot of the resulting densities of the dust in the three size bins, 0.1–10, 100, and 1000 μm . The larger grains show stronger settling and show the characteristic motions induced by the VSI. The local dust-to-gas mass ratio for the three bins is presented in Figure 9. The plot shows that the highest dust concentration and dust density is present for the largest grain size bin. We note that similar structures in the dust density were reported by Lorén-Aguilar & Bate (2015). They presented a new kind of instability caused by the combination of dust settling and the resulting vertical entropy gradient, which they found in gas and dust hydrodynamical simulations.

We then compute the opacity of the dust in each bin, assuming the grains are made of 62.5% silicate and 37.5% graphite, using the tool MieX (Wolf & Voshchinnikov 2004). More details on the opacity calculation and the optical properties we use can be found in Appendix C. We pass the results into RADMC-3D to compute synthetic images as in

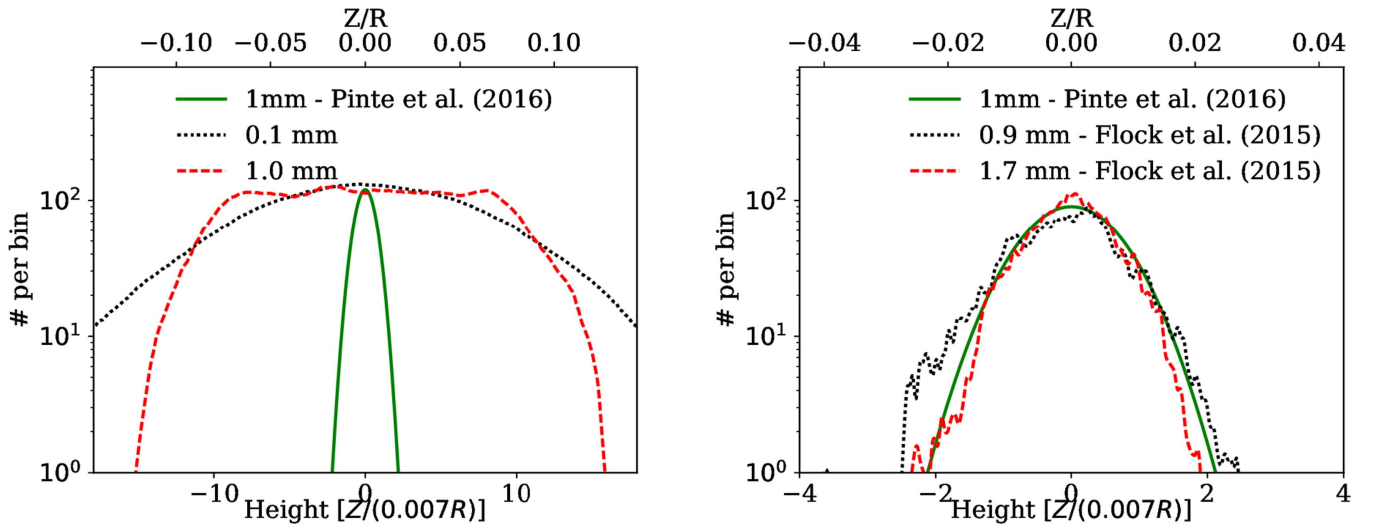


Figure 6. Time- and space-averaged vertical distribution of two grain sizes. Left: grain data set for the model M3 taken at 30 au. Right: grain distribution for the magnetized disk model by Flock et al. (2015) and the grain data set by Ruge et al. (2016) taken at 45 au. For both plots, the green line shows the best-fit constraints from the systems HL Tau by Pinte et al. (2016) assuming $H/R = 0.007$.

Figure 10, where model M3 is viewed face-on at a wavelength of 0.87 mm. We multiply the intensity by r^2 to focus on the appearance of local dust density variations. The strongest features come from radial variations in the density of the largest grains, which are concentrated into rings with azimuthal structure superimposed, similar to Stoll & Kley (2016). The smaller grains are much more smoothly distributed, and contribute little to these features. Note that the grid is carried over from the radiation hydrodynamical calculation, and all features present there are resolved here. In the bottom panel of Figure 10, we show the same synthetic image convolved with a Gaussian filter of width 5 au ($0''.0357$ at 140 pc) to mimic an observation from ALMA. At this resolution, the small-scale features are smoothed out.

The results show that local concentration of dust material could still be hidden in the large-scale structure that is usually observed. This could also be the case for the observation of HL Tau, which shows concentric rings (ALMA Partnership et al. 2015). We note that for our VSI turbulent models we do not observe any long-term pressure maximum that would cause a high concentration of particles. Instead, the concentrations observed in the VSI simulations arise because of temporary concentration of grains in short-lived, transient perturbations to the disk vorticity induced by the VSI, as described in Richard et al. (2016).

4. Discussion

4.1. Mass Accretion Rate

The median rate of mass accretion onto normal classical T Tauri stars is about $10^{-8} M_{\odot} \text{ yr}^{-1}$ (Najita et al. 2015; Kim et al. 2016). The Reynolds stresses in our VSI calculations yield much smaller mass flow rates. We estimate the mass accretion rate using the approximation of $\dot{M} = 3\pi\Sigma\nu$, which is valid in steady-state and if $r \gg R_*$. At 100 au we approximate the mass accretion rate to $\dot{M} \approx 2 \times 10^{-10} M_{\odot} \text{ yr}^{-1}$ using $\nu = \alpha H^2 \Omega_K$ with $\alpha = 3.8 \times 10^{-5}$ and $H(100 \text{ au}) = 14 \text{ au}$ for both of our models.

Recent best-fit estimates from TW Hya by Herczeg & Hillenbrand (2008), Brickhouse et al. (2012) determine a mass

accretion rate of $10^{-9} M_{\odot} \text{ yr}^{-1}$. Assuming a constant mass accretion rate over radius, and taking the best-fit models of the gas surface density at 100 au to around 5 g cm^{-2} , $H(100 \text{ au}) = 9 \text{ au}$ and $M_* = 0.87 M_{\odot}$ (Menu et al. 2014; van Boekel et al. 2017), we determine a value of around $\alpha^{\text{TW Hya}} = 4 \times 10^{-4}$. Such a value is also preferred in terms of the strength of the dust mixing in their models (van Boekel et al. 2017).

For the more massive disk around HD 163296, the mass accretion rate was determined recently by Mendigutía et al. (2013) to be $4.5 \times 10^{-7} M_{\odot} \text{ yr}^{-1}$. Using the same estimate as above with the parameter 5 g cm^{-2} , $H(100 \text{ au}) = 11 \text{ au}$ and $M_* = 0.87 M_{\odot}$ (Isella et al. 2016) yield a value of $\alpha^{\text{TW Hya}} = 7.6 \times 10^{-2}$. However, in this system, such a high value can be ruled out due to the good visibility of the gaps (Isella et al. 2016).

Even given these uncertainties for the estimates of the gas surface density and the fact that the mass accretion rates vary over radius and time, we think that it is unlikely that the VSI alone can explain the observed accretion rates. At best, given the current results and constraints, the VSI could support the mass accretion rate at larger radii where the conditions required for short thermal equilibration timescales are fulfilled. In contrast, magnetized disk models predict a turbulent stress level two orders of magnitude higher at similar distances from the star (Flock et al. 2015; Simon et al. 2015b).

4.2. Kinematic Constraints by Observations and VSI Kinematic

Observations of the close-by young protoplanetary disk TW Hya with ALMA by Teague et al. (2016) have demonstrated the difficulty of constraining the exact value of the gas turbulence in the disk by means of molecular line observations. There are two main limitations to determining the gas kinematics from the broadened line profile. The first limitation comes from the fact that the thermal broadening and the turbulent broadening are difficult to disentangle. In the work by Flaherty et al. (2015, 2017), and also pointed out by Simon et al. (2015a), they are able to disentangle these effects by viewing the molecular line in the spatial domain. However, we note that if the thermal and turbulence structure are unknown,

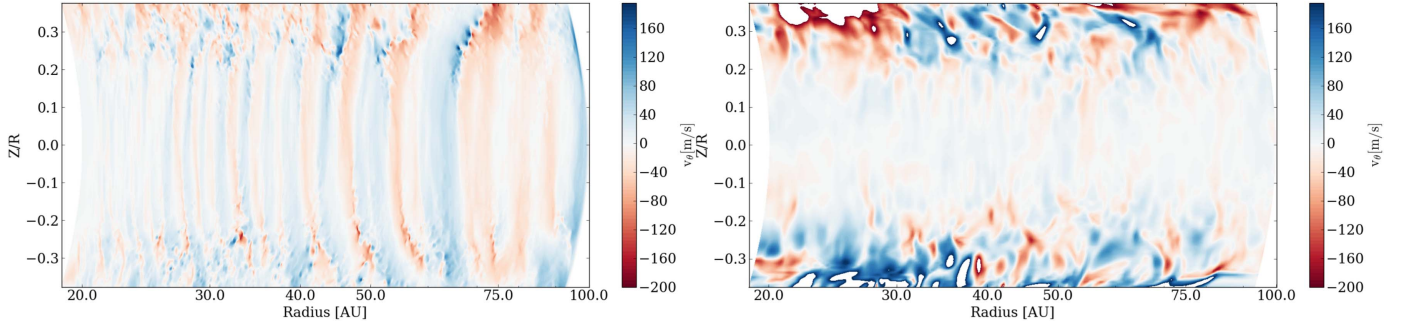


Figure 7. Left: snapshot of the vertical velocity component in the R - Z/R plane for the model M3 taken after 400 inner orbits. Right: snapshot of the vertical velocity component for the magnetized disk model by Flock et al. (2015). Both slices are taken at $\phi = 0$.

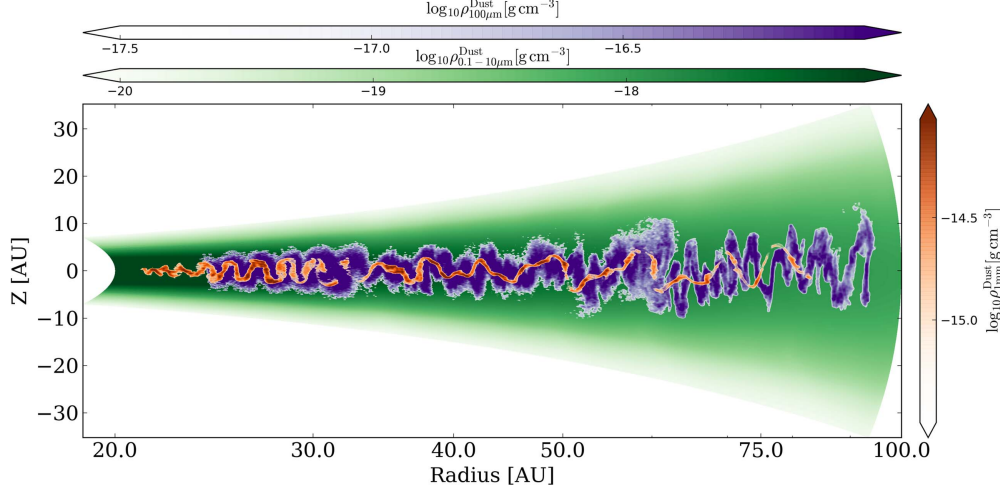


Figure 8. Azimuthally averaged dust density for three representative dust grain bins in the R - Z/R plane for model M3, taken after 470 inner orbits (70 orbits of dust evolution).

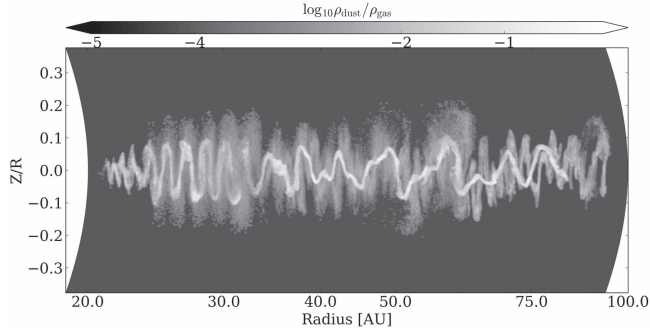


Figure 9. Azimuthally averaged dust-to-gas mass ratio in the R - Z/R plane for model M3, taken after 470 inner orbits (70 orbits of dust evolution).

the systematic error in determining the turbulent broadening could be as high as the broadening itself. The second limitation comes from the flux calibration error. Teague et al. (2016) pointed out that the flux calibration error alone limits the accuracy with which the turbulent broadening component can be determined. Improved observations and modeling are needed to further constrain the kinematics.

We also emphasize that the turbulent structures caused by the VSI are clearly different from the turbulence generated by the MRI. While the MRI generates a turbulent structure that would produce a thermal-type line-broadening (Simon et al. 2015a), this is not straightforward for the VSI. Particularly, the large-scale

motions might produce a broadening type that could be different and depend on the inclination of the disk. Further detailed line transfer models should be done to constrain the detailed effects of the VSI turbulence on the line shape. Particularly, spatially resolved observations would allow one to obtain the radial profiles of the turbulent line-broadening to further constrain the underlying mechanism triggering turbulence in disks.

4.3. Dust Feedback and VSI Activity

We briefly want to address the important implications the results could have regarding dust motion. The radiation hydrodynamical simulations of dust and gas show coherent motions for the large grains. They naturally lead to very low relative velocities between two neighboring large grains. This could suppress fragmentation and lead to much larger grain sizes that would then totally decouple from the gas motion (Okuzumi et al. 2012). Second, the local dust density can become quite large for the mm-sized grains. In the 3D data set shown in Figure 9, we found the maximum dust-to-gas mass ratio in one single cell to be 2.3. This substantially increases the collision rate and thus decreases the grain growth timescale (Brauer et al. 2008; Birnstiel et al. 2012). We expect the dust drag force to dominate at the midplane region and therefore we expect only minor effects on the VSI activity. However, the dust drag could affect the dynamics at the midplane region. Future simulations that include the dust feedback onto the gas are needed to further constrain these effects.

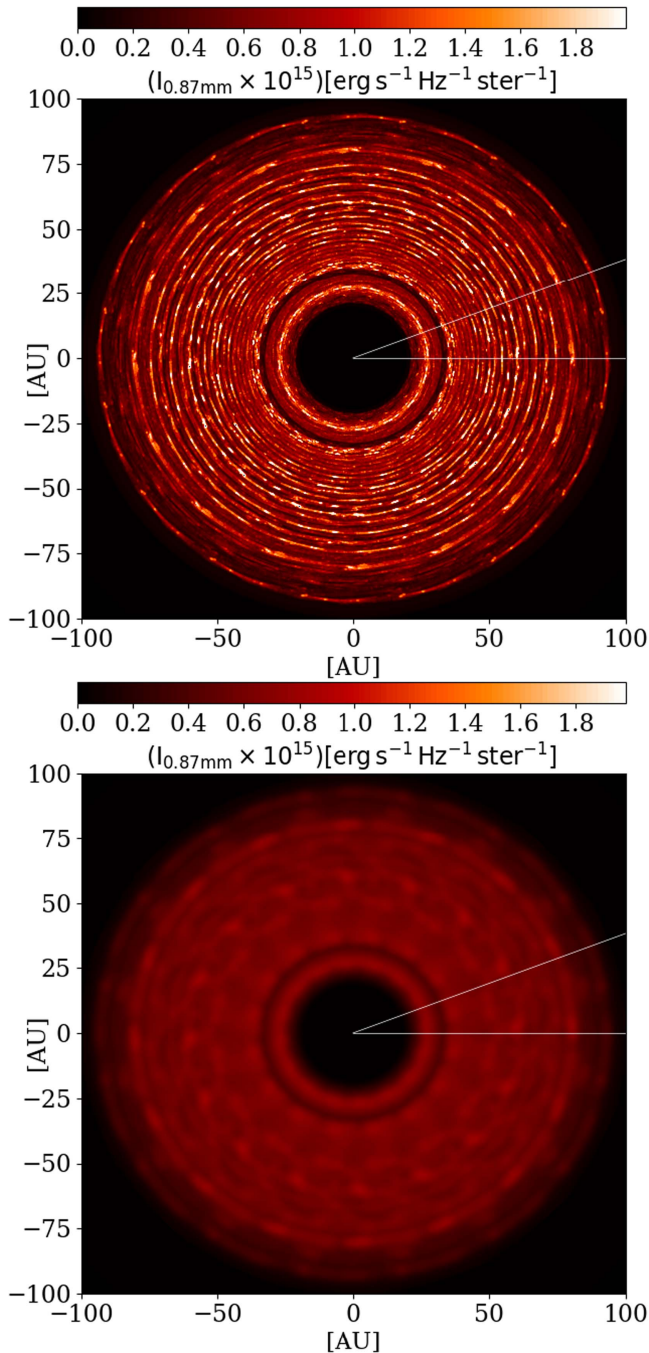


Figure 10. Top: synthetic 0.87 mm image of model M3 viewed face-on. Bottom: same image convolved with a 2D Gaussian of half-width 5 au. The white lines indicate the azimuthal extent of the calculation's domain, $22^\circ 5'$. The rest of the image is generated by applying periodic azimuthal boundary conditions.

5. Summary and Conclusion

We have performed 3D radiation hydrodynamical simulations of protoplanetary disks' outer regions, resolving all three-dimensions with about 70 cells per density scale height. The star and disk parameters are those of a typical T Tauri system. The disk absorbs and reradiates the starlight with opacities computed using Mie theory, and dominated by small dust grains. We consider the dust-to-gas mass ratios of small grains of 10^{-4} and 10^{-3} , leading to thermal equilibration rapid

enough for the VSI to operate. We also track the movements of 0.1 and 1 mm grains embedded in the two model disks. Our main findings on the gas and dust dynamics are as follows.

1. The VSI saturates in turbulence what remains in quasi-steady-state out to at least 1600 inner orbits (143 outer orbits). The mass-weighted stress-to-pressure ratio is about 4×10^{-5} at both dust fractions. The turbulent gas motions have a rms Mach number $\sim 1\%$ at the midplane, and $\sim 10\%$ in the corona.
2. The VSI produces clear vertical bulk motions, which loft the 1 mm grains to about one gas scale height from the midplane. This is much higher than the accretion stresses would imply under isotropic turbulent diffusion, thanks to the anisotropy. The characteristic radial extent of the upward- or downward-moving gas parcels is also about one scale height.

Furthermore, we compared our models with observational constraints, and also compared with results from a magnetized disk model by Flock et al. (2015) and Ruge et al. (2016). The main findings are as follows.

1. Turbulent speeds at the disk midplane in both the magnetized and non-magnetized models are broadly consistent with upper limits on turbulent line-broadening measured in the TW Hya disk at 0.2 times the sound speed c_s (Teague et al. 2016) and in HD 163296 at $0.04c_s$ (Flaherty et al. 2015). The VSI turbulence remains below the upper limit of $0.2c_s$ over the whole domain, while the magnetized disk models' corona violates this constraint above height $Z = 0.2R$. The molecular line observations are sensitive to regions outside 10 au, and can trace the interior $Z \ll 0.2R$ as in HD 142527 (Perez et al. 2015) or corona $Z \sim 0.2R$ as in TW Hya (Teague et al. 2016), depending on the disk surface density and the molecule.
2. The mm-sized particles' scale height in the VSI turbulence is too great to be consistent with the well-separated rings of millimeter thermal emission observed in the inclined HL Tau disk. Such thick rings would overlap with one another along the projected minor axis (Isella et al. 2016; Pinte et al. 2016). In contrast, the grains trapped near the dead zone edge in the magnetized calculation well-match the scale height $H_{\text{dust}} = 0.007R$ that Pinte et al. (2016) inferred for the mm grains in HL Tau.
3. Synthetic images made from our global radiation hydrodynamical results show concentric rings much narrower than the gas scale height. When convolved with a nominal telescope beam, the rings appear wider and their amplitude is reduced. The rings are transient, with the grains experiencing neither long-term trapping nor net radial concentration.
4. The VSI turbulent Reynolds stress is two order of magnitude less than needed to explain the measured rates of accretion onto the stars. Angular momentum is thus probably not extracted purely by VSI.

Overall, these results are consistent with a picture in which magnetic forces drive the accretion flow and suppress the VSI, but the magnetic activity is modulated by non-ideal MHD effects. Thus, detecting magnetic fields and measuring their strengths would be extremely useful for understanding protostellar disks' dynamics and evolution. Furthermore, future

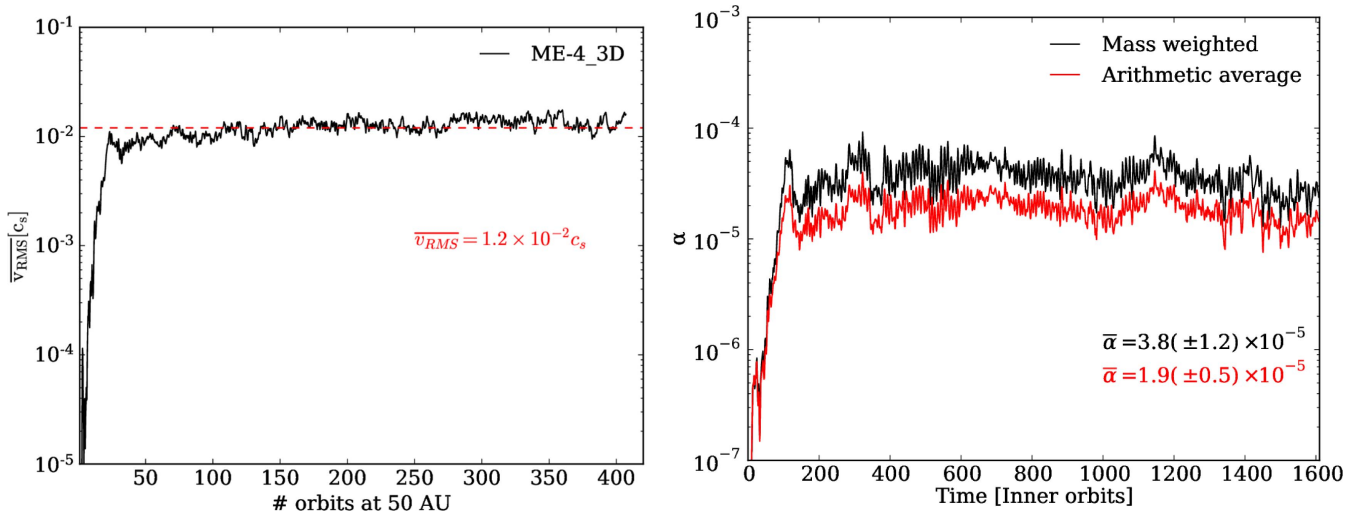


Figure 11. Left: long-term time evolution of the mass-weighted turbulent velocity over radius for model M4. Time-averaged values are annotated using a red dashed line and red labeling. Right: corresponding time evolution of the stress-to-pressure ratio α , using the approach of mass-weighted values (black) and using an arithmetic average (red).

modeling should treat the grains’ movements through the gas, because most of the solid material in protostellar disks’ outer regions shows significant settling.

The authors thank Sebastian Wolf and Hubert Klahr for their helpful discussions and comments on the project. We thank Andrea Mignone for supporting and advising us with the newest PLUTO code. We thank Andrea Isella for his comments on the radiation transfer post-processing. Parallel computations have been performed on the zodiac supercomputer at JPL. For this work, Mario Flock received partial funding from the European Research Council under the European Union’s Seventh Framework Programme (FP7/2007–2013)/ERC grant agreement no. 258729. This research was carried out in part at the Jet Propulsion Laboratory, California Institute of Technology, under a contract with the National Aeronautics and Space Administration and with the support of the NASA Exoplanet Research program via grant 14XRP14_20153. Richard Nelson acknowledges support from STFC through the grants ST/P000592/1 and ST/M001202/1. Gesa H.-M. Bertrang acknowledges financial support from CONICYT through FONDECYT grant 3170657, as well as by the Millennium Science Initiative (Chilean Ministry of Economy), through grant Nucleus RC13007. Wladimir Lyra acknowledges the support of the Space Telescope Science Institute through grant *HST*-AR-14572 and the NASA Exoplanet Research Program through grant 16-XRP16 20065. This research was supported in part by the National Science Foundation under grant No. NSF PHY-1125915. Government sponsorship is acknowledged.

Appendix A

Long-term Turbulent Evolution and Calculation of the Reynolds Stress

The long-term turbulent evolution of the disk was calculated for model M4. To capture the growth of modes with longer growth times we run the model for 1610 inner orbits (143 outer orbits). The detailed growth of the turbulent velocities is shown

in the left panel of Figure 11. At 30 local orbits the simulation reaches a clear steady-state showing mass-weighted turbulent velocities at around 1% of the sound speed. The long-term evolution of the stress-to-pressure ratio is shown in the right panel of Figure 11. The simulation shows a clear steady-state. The turbulent velocity and the stress-to-pressure ratio are mass-weighted.

To compare our results for the calculation of the Reynolds stress we present here another approach to calculate the time- and space-averaged stress-to-pressure ratio. For this second approach we follow the calculation described by Nelson et al. (2013). For this, we calculate the Reynolds stress $T_{r\phi}(r, \theta) = \rho \delta v_r \delta v_\phi$ in the 2D plane (r, θ) by averaging along an azimuth. We then define a density-weighted, azimuthally and vertically averaged mean pressure $\bar{P}(r)$ at each radius r , which then allows us to express the stress-to-pressure ratio as $\alpha(r, \theta) = T_{r\phi}(r, \theta) / \bar{P}(r)$. In the right panel of Figure 11, we compare the results. The arithmetic average results in a slightly smaller value of the stress-to-pressure ratio. This can be explained as the value of α slightly increases with radius. As there is more mass stored at the outer radii, the mass-weighted value is slightly higher. Overall, the value of the stress-to-pressure ratio proved to be small and slightly lower compared to what was found in previous global isothermal (Nelson et al. 2013) and recent global radiation hydrodynamic models (Stoll & Kley 2016), and probably depends in detail on the thermodynamic and opacity models adopted. Certainly, further high-resolution studies of the VSI are needed to constrain the level of turbulence, especially due to the fact that the fastest growing modes have very short wavelengths and usually are limited by the grid resolution (Barker & Latter 2015).

Appendix B

Vertical Bulk Motions by the VSI

In this appendix we present snapshots of the grain distribution after 50 inner orbits of evolution. Figure 12 shows the snapshot of the evolution of 50 inner orbits. For the two grain sizes, the vertical bulk motions are able to lift the

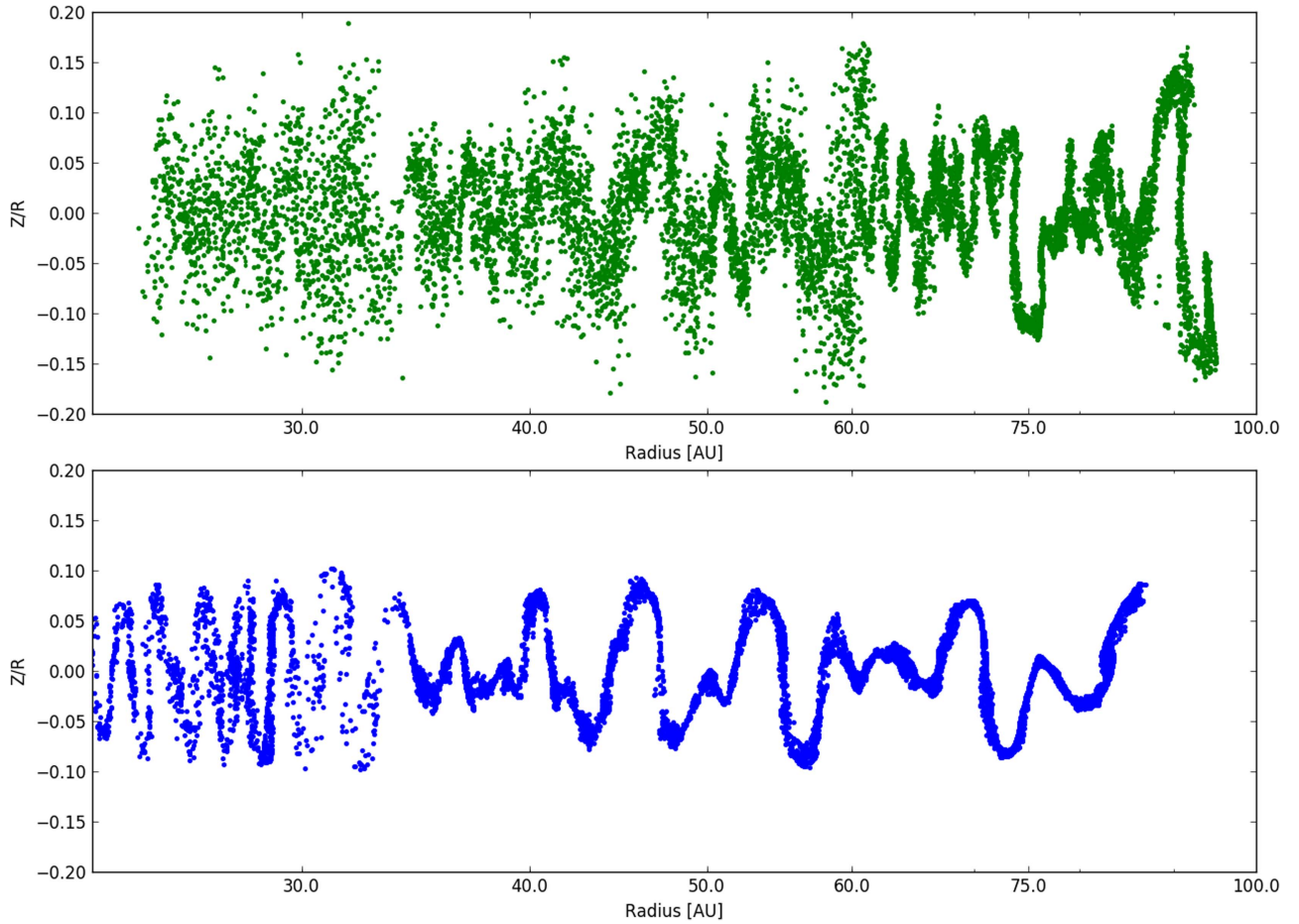


Figure 12. Snapshot of the grain distribution in the R - Z/R plane for the 0.1 mm grains (top) and for the 1 mm grains (bottom) after 50 inner orbits of evolution of model M3. Every fiftieth particle from the total data set is shown.

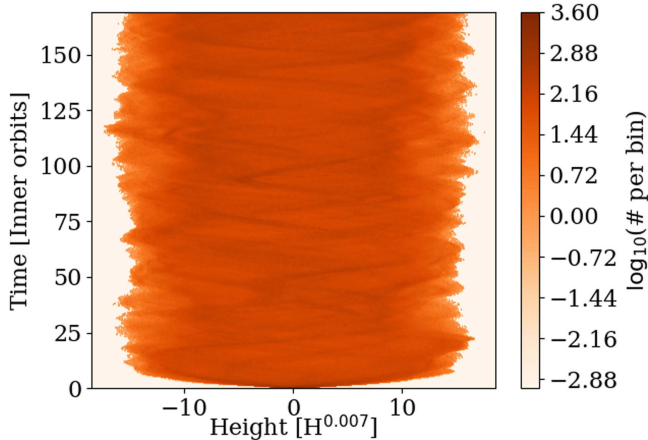


Figure 13. Time evolution of the 1 mm grain vertical distribution of model M3.

grains ± 1 scale height upward and downward the midplane. These motions are responsible for the effective large-scale height described in Section 3.3.

In the following we will check how fast the millimeter grains reach an equilibrium state. Figure 13 shows the vertical distribution of mm grains over time in the radial extent from 25 to 35 au. The particles quickly reach into an equilibrium state. To determine the vertical profile shown in Figure 6, we have taken a time average starting after 20 inner orbits.

Appendix C



Calculation of the Opacity and RT Post-processing

To determine the opacity we use the tool MieX (Wolf & Voshchinnikov 2004) using the optical data by Weingartner & Draine (2001). The dust material has a composition of 62.5% silicate, 25% perpendicular graphite, and 12.5% parallel graphite. We determine three characteristic dust bins. The first bin uses minimum and maximum grain sizes of $a_{\min} = 0.1 \mu\text{m}$ and $a_{\max} = 10 \mu\text{m}$, with a size distribution exponent of -3.5 . The second and third size bins use single dust grain sizes of 0.1 and 1 mm. The wavelength grid is the same to determine the opacity and to calculate the RT modeling. From MieX we obtain the scattering and absorption efficiency factors Q_{sca} and Q_{abs} . Together with the corresponding cross section $C = Q\pi a_{\text{eff}}^2$, we can determine the opacity per gram of dust using

$$\kappa_{\lambda} = \frac{Q^{3/2}}{C^{1/2}} \frac{\sqrt{\pi}}{\rho_d} \frac{3}{4}, \quad (18)$$

for each wavelength. For the RADMC-3D setup run we use 10^9 photon packages. We apply the same grid in RADMC-3D as was used for the global simulation run. We use three individual dust grain bins and we determine the particle density from the corresponding particle distribution.

ORCID iDs

Mario Flock  <https://orcid.org/0000-0002-9298-3029>
 Neal J. Turner  <https://orcid.org/0000-0001-8292-1943>
 Wladimir Lyra  <https://orcid.org/0000-0002-3768-7542>
 Richard Teague  <https://orcid.org/0000-0003-1534-5186>

References

- ALMA Partnership, Brogan, C. L., Pérez, L. M., et al. 2015, *ApJL*, **808**, L3
 Andrews, S. M., Wilner, D. J., Zhu, Z., et al. 2016, *ApJL*, **820**, L40
 Arlt, R., & Urpin, V. 2004, *A&A*, **426**, 755
 Armitage, P. J. 2015, arXiv:1509.06382
 Bae, J., Nelson, R. P., Hartmann, L., & Richard, S. 2016, *ApJ*, **829**, 13
 Bai, X.-N. 2011, *ApJ*, **739**, 50
 Bai, X.-N. 2014, *ApJ*, **791**, 72
 Balbus, S. A., & Hawley, J. F. 1991, *ApJ*, **376**, 214
 Balbus, S. A., & Hawley, J. F. 1998, *RvMP*, **70**, 1
 Barker, A. J., & Latter, H. N. 2015, *MNRAS*, **450**, 21
 Bertrang, G. H.-M., Flock, M., & Wolf, S. 2017, *MNRAS*, **464**, L61
 Bertrang, G. H.-M., & Wolf, S. 2017, *MNRAS*, **469**, 2869
 Birstiel, T., Klahr, H., & Ercolano, B. 2012, *A&A*, **539**, A148
 Brauer, F., Dullemond, C. P., & Henning, T. 2008, *A&A*, **480**, 859
 Brickhouse, N. S., Cranmer, S. R., Dupree, A. K., et al. 2012, *ApJL*, **760**, L21
 Cameron, A. G. W., & Pine, M. R. 1973, *Icar*, **18**, 377
 Carrasco-González, C., Henning, T., Chandler, C. J., et al. 2016, *ApJL*, **821**, L16
 Decampli, W. M., Cameron, A. G. W., Bodenheimer, P., & Black, D. C. 1978, *ApJ*, **223**, 854
 Dullemond, C. P. 2012, RADMC-3D: A multi-purpose radiative transfer tool, Astrophysics Source Code Library, ascl:1202.015
 Dzyurkevich, N., Turner, N. J., Henning, T., & Kley, W. 2013, *ApJ*, **765**, 114
 Fedele, D., Carney, M., Hogerheijde, M. R., et al. 2017, *A&A*, **600**, A72
 Flaherty, K. M., Hughes, A. M., Rose, S. C., et al. 2017, *ApJ*, **843**, 150
 Flaherty, K. M., Hughes, A. M., Rosenfeld, K. A., et al. 2015, *ApJ*, **813**, 99
 Flock, M., Fromang, S., González, M., & Commerçon, B. 2013, *A&A*, **560**, A43
 Flock, M., Ruge, J. P., Dzyurkevich, N., et al. 2015, *A&A*, **574**, A68
 Fricke, K. 1968, *ZAp*, **68**, 317
 Goldreich, P., & Schubert, G. 1967, *ApJ*, **150**, 571
 Gräfe, C., Wolf, S., Guilloteau, S., et al. 2013, *A&A*, **553**, A69
 Guilloteau, S., Dutrey, A., Wakelam, V., et al. 2012, *A&A*, **548**, A70
 Herczeg, G. J., & Hillenbrand, L. A. 2008, *ApJ*, **681**, 594
 Hughes, A. M., Wilner, D. J., Andrews, S. M., Qi, C., & Hogerheijde, M. R. 2011, *ApJ*, **727**, 85
 Isella, A., Guidi, G., Testi, L., et al. 2016, *PhRvL*, **117**, 251101
 Kataoka, A., Muto, T., Momose, M., et al. 2015, *ApJ*, **809**, 78
 Kataoka, A., Tsukagoshi, T., Momose, M., et al. 2016, *ApJL*, **831**, L12
 Kataoka, A., Tsukagoshi, T., Pohl, A., et al. 2017, *ApJL*, **844**, L5
 Kim, K. H., Watson, D. M., Manoj, P., et al. 2016, *ApJS*, **226**, 8
 Klahr, H., & Hubbard, A. 2014, *ApJ*, **788**, 21
 Klahr, H. H., & Bodenheimer, P. 2003, *ApJ*, **582**, 869
 Lesur, G., & Papaloizou, J. C. B. 2010, *A&A*, **513**, A60
 Lesur, G. R. J., & Latter, H. 2016, *MNRAS*, **462**, 4549
 Levermore, C. D., & Pomraning, G. C. 1981, *ApJ*, **248**, 321
 Lin, M.-K., & Youdin, A. N. 2015, *ApJ*, **811**, 17
 Liu, Y., Henning, T., Carrasco-Gonzalez, C., et al. 2017, arXiv:1708.03238
 Liu, Y., Madlener, D., Wolf, S., Wang, H., & Ruge, J. P. 2012, *A&A*, **546**, A7
 Lorén-Aguilar, P., & Bate, M. R. 2015, *MNRAS*, **453**, L78
 Lyra, W. 2014, *ApJ*, **789**, 77
 Macías, E., Anglada, G., Osorio, M., et al. 2017, *ApJ*, **838**, 97
 Madlener, D., Wolf, S., Dutrey, A., & Guilloteau, S. 2012, *A&A*, **543**, A81
 Malygin, M. G., Klahr, H., Semenov, D., Henning, T., & Dullemond, C. P. 2017, arXiv:1704.06786
 Marcus, P. S., Pei, S., Jiang, C.-H., et al. 2015, *ApJ*, **808**, 87
 Marcus, P. S., Pei, S., Jiang, C.-H., & Hassanzadeh, P. 2013, *PhRvL*, **111**, 084501
 Masset, F. 2000, *A&AS*, **141**, 165
 Mendigutía, I., Brittain, S., Eiroa, C., et al. 2013, *ApJ*, **776**, 44
 Menu, J., van Boekel, R., Henning, T., et al. 2014, *A&A*, **564**, A93
 Mignone, A., Bodo, G., Massaglia, S., et al. 2007, *ApJS*, **170**, 228
 Mignone, A., Zanni, C., Tzeferacos, P., et al. 2012, *ApJS*, **198**, 7
 Najita, J. R., Andrews, S. M., & Muzerolle, J. 2015, *MNRAS*, **450**, 3559
 Nelson, R. P., Gressel, O., & Umurhan, O. M. 2013, *MNRAS*, **435**, 2610
 Okuzumi, S., Tanaka, H., Kobayashi, H., & Wada, K. 2012, *ApJ*, **752**, 106
 Papaloizou, J. C. B., & Pringle, J. E. 1984, *MNRAS*, **208**, 721
 Perez, S., Casassus, S., Ménard, F., et al. 2015, *ApJ*, **798**, 85
 Pinte, C., Dent, W. R. F., Ménard, F., et al. 2016, *ApJ*, **816**, 25
 Pohl, A., Pinilla, P., Benisty, M., et al. 2015, *MNRAS*, **453**, 1768
 Pringle, J. E. 1981, *ARA&A*, **19**, 137
 Richard, S., Nelson, R. P., & Umurhan, O. M. 2016, *MNRAS*, **456**, 3571
 Ruge, J. P., Flock, M., Wolf, S., et al. 2016, *A&A*, **590**, A17
 Salmeron, R., & Wardle, M. 2008, *MNRAS*, **388**, 1223
 Sauter, J., Wolf, S., Launhardt, R., et al. 2009, *A&A*, **505**, 1167
 Schegerer, A. A., Wolf, S., Hummel, C. A., Quanz, S. P., & Richichi, A. 2009, *A&A*, **502**, 367
 Schegerer, A. A., Wolf, S., Ratzka, T., & Leinert, C. 2008, *A&A*, **478**, 779
 Shakura, N. I., & Sunyaev, R. A. 1973, *A&A*, **24**, 337
 Simon, J. B., Hughes, A. M., Flaherty, K. M., Bai, X.-N., & Armitage, P. J. 2015a, *ApJ*, **808**, 180
 Simon, J. B., Lesur, G., Kunz, M. W., & Armitage, P. J. 2015b, *MNRAS*, **454**, 1117
 Stoll, M. H. R., & Kley, W. 2016, *A&A*, **594**, A57
 Tazaki, R., Lazarian, A., & Nomura, H. 2017, *ApJ*, **839**, 56
 Teague, R., Guilloteau, S., Semenov, D., et al. 2016, *A&A*, **592**, A49
 Turner, N. J., Benisty, M., Dullemond, C. P., & Hirose, S. 2014, *ApJ*, **780**, 42
 Umurhan, O. M., Shariff, K., & Cuzzi, J. N. 2016, *ApJ*, **830**, 95
 Urpin, V. 2003, *A&A*, **404**, 397
 Urpin, V., & Brandenburg, A. 1998, *MNRAS*, **294**, 399
 van Boekel, R., Henning, T., Menu, J., et al. 2017, *ApJ*, **837**, 132
 Wardle, M. 2007, *Ap&SS*, **311**, 35
 Weingartner, J. C., & Draine, B. T. 2001, *ApJ*, **548**, 296
 Wolf, S., Padgett, D. L., & Stapelfeldt, K. R. 2003, *ApJ*, **588**, 373
 Wolf, S., Schegerer, A., Beuther, H., Padgett, D. L., & Stapelfeldt, K. R. 2008, *ApJL*, **674**, L101
 Wolf, S., & Voshchinnikov, N. V. 2004, *CoPhC*, **162**, 113